JOURNAL OF PROPULSION AND POWER
Vol. 12, No. 4, July–August 1996

Unsteady Vorticity Generation and Evolution in a Model of a Solid Rocket Motor

Kadir Kirkkopru,* David R. Kassoy,† and Qing Zhao‡
University of Colorado, Boulder, Colorado 80309

The cylindrical, axisymmetric Navier–Stokes equations are solved numerically to study the generation and evolution of vorticity in an injection-induced transient shear flow. An initially steady internal flowfield driven by constant sidewall injection is disturbed by positive transient sidewall injection, which simulates the unsteady mass input from propellant burning variations. The disturbance amplitude is as large as that of the steady sidewall injection to ensure that nonlinear effects influence the vorticity field evolution. Initial value solutions show that relatively intense vorticity is generated at the sidewall and eventually fills the cylinder with a rotational flow. Although the pressure response is essentially that found in acoustic stability theory, the axial and radial velocity components contain large local radial velocity gradients that cannot be predicted from acoustic theory alone.

I. Introduction

SOLID propellant combustion in a rocket motor generates gaseous products that induce a low axial Mach number [$M = \mathcal{O}(10^{-2}-10^{-1})$], large flow Reynolds number [$Re = \mathcal{O}(10^4-10^6)$] internal shear flow in a cylindrical chamber where the aspect ratio is $\delta >> 1$. Inert flows with these characteristics can be generated by injecting gas through the porous sidewall of a cylinder. Flow transients are then induced by specified time-dependent boundary conditions applied on some surface or on the exit plane. The complete time-dependent shear flow is now known to include vorticity distributions,[1–8] as well as the more familiar acoustic disturbances studied by many investigators in the past.[9–12]

Brown et al.[1,2] and Brown and Shaeffer[3] conducted laboratory experiments in a cold flow rocket motor chamber analogue. Velocity measurements taken along and across the cylindrical chamber show that there is a significant unsteady rotational flow component present everywhere. This type of vorticity is seen also in the study by Vuillot and Avalon[4] who used computational methods to solve the compressible Navier–Stokes equations in a channel with constant sidewall mass injection. Both results demonstrate that for sufficiently large wall injection rates unsteady vorticity need not be confined to thin viscous acoustic boundary layers adjacent to the injecting wall, like those observed in the numerical studies of Baum and Levine[13] and Baum[14] and in the acoustic boundary-layer analysis of Flandro.[5]

Flandro and Roach[15] and Smith et al.[16] describe numerical simulations of the Brown et al.[1,2] experiments. Significant radial gradients in the axial velocity are seen about halfway out toward the centerline. They capture the qualitative features of the spatial vorticity distributions observed by Brown et al.[1,2]

Flandro and Roach[15] describe an initial attempt at developing an analytically based model of the Brown and co-worker experiments. A more complete version is given in Flandro,[17] where a theory is developed for coexisting transient vorticity and acoustic waves throughout a cylindrical chamber. The steady, inviscid rotational Culick[18] solution, associated with a uniform injection Mach number $M_i << 1$, is disturbed by a smaller $\mathcal{O}(\varepsilon)$ acoustic velocity that varies harmonically in time. Perturbation methods are used to derive inviscid, linear, small disturbance equations for the rotational part of the axial velocity. The momentum equation itself can be used to show that the amplitude of the vorticity generated at the injection surface is $\mathcal{O}(\varepsilon/M_i^2)$ relative to the vorticity associated with the steady Culick[18] profiles. Hence, for sufficiently large values of ε, the transient vorticity can be more intense than that of the steady Culick velocity components. Calculated axial velocity variation with radius is qualitatively similar to the spatial oscillations observed experimentally by Brown et al.[1,2]

Tseng and Yang[19] and Tseng et al.[7] provide a computational model for a premixed laminar flame adjacent to a cylindrical porous surface through which a combustible mixture is injected. The flame is a surrogate for solid propellant combustion in a rocket chamber. Prescribed boundary disturbances are the sources of transients in the flowfield. In this reactive model of a chamber, flow vorticity appears in the vicinity of the wall and the adjacent flame.

Roh and Yang[20] have done a similar computation for combustion processes associated with double-base solid propellants. Longer run times and better spatial resolution lead to the appearance of vorticity through 75% of the half-height of the rectangular chamber.

Zhao et al.[21] as well as Zhao and Kassoy[8] use a systematic asymptotic analysis to formulate an initial boundary value description of vorticity production in a low Mach number ($M << 1$), weakly viscous internal flow ($Re >> 1$), sustained by mass addition through the sidewall of a long, narrow cylinder ($\delta >> 1$). A hard blowing condition (characteristic injection speed is much larger than the characteristic axial speed divided by $Re^{1/2}$ (Ref. 22)) is used. An $\mathcal{O}(M)$ axial acoustical disturbance, generated by a prescribed harmonically time-dependent closed endwall velocity, interacts with the basically inviscid rotational steady flow to produce unsteady vorticity at the injecting sidewall. Baroclinicity and volume dilatation are higher-order sources of unsteady vorticity production in this nearly isothermal flow. The complete axial velocity is found from a superposition of three components of equal magnitude. First, the steady component is described by a weakly rotational, steady solution to inviscid Euler equations known by Culick.[18] Secondly, there is a planar irrotational acoustic field,

Received Dec. 27, 1994; revision received Feb. 19, 1995; accepted for publication Feb. 20, 1996.

*Research Associate, Program in Applied Math; currently at Department of Mechanical Engineering, Istanbul Technical University, Istanbul, Turkey.

†Professor, Department of Mechanical Engineering. Member AIAA.

‡Graduate Student. Department of Mechanical Engineering; currently at Applicon, Inc., Boulder, CO 80301.

derived from a traditional linear wave equation that satisfies boundary conditions at the closed and open ends of the cylinder. Finally, when $Re = \mathcal{O}(\delta^2/M^2)$, the strongly rotational, weakly viscous, nonlinear component varies simultaneously on the length scale of the tube radius $\mathcal{O}(1)$ and on an $\mathcal{O}(M)$ smaller scale similar to those described in the study by Flandro and Roach.[15] Mathematical formulas are used to prove that the vorticity is generated at the wall by an interaction between the injected fluid and the time-dependent axial pressure gradient. It is then diffused on the short $\mathcal{O}(M)$ radial length scale and convected subsequently toward the axis by the radial component of the injection-induced flowfield. Initially, the intense wall-generated vorticity is separated from the weakly rotational flow of the Culick[18] solution by a sharply defined front that convects in the radial direction at the local radial speed. Eventually, the wall-generated rotational flow fills the entire cylinder.

Computational methods are used by Kirkkopru et al.[6] to provide qualitative supporting evidence for the solutions described in Zhao et al.[21] In this case the driving disturbance is a harmonic pressure transient applied on the exit plane of the cylinder, like that used by Vuillot and Avalon.[4] Grid size and spatial distributions are chosen to accommodate the small length scale velocity variations throughout the cylinder known from the study by Zhao et al.[21] In analogy with the analytical effort, the unsteady rotational component of the axial velocity is extracted from the numerically generated total value. The initial-boundary value solution properties and characteristics are similar to those found from the asymptotic analysis in Ref. 21.

The objective of the present work is to compute unsteady vorticity production and evolution in a finite cylinder with spatially distributed, transient injection from the sidewall. The latter mimics unsteady burning of a solid propellant surface. The two–four method[23] is used to obtain solutions to the unsteady, compressible Navier–Stokes equations in a cylindrical axisymmetric geometry. Parametric values for Re, M, and δ are chosen to ensure that the hard blowing condition of Cole and Aroesty[22] ($\delta^2/Re \ll 1$) is met and that the analytically derived weakly viscous condition $Re = \mathcal{O}(\delta^2/M^2)$ is satisfied. Grid points are distributed in the radial direction to resolve $\mathcal{O}(M)$ length scale velocity variations throughout the cylinder as predicted by the asymptotic study.[21] The unsteady rotational component of the axial velocity u_V, extracted from the numerical solutions, is used to describe the generation and evolution of the nonlinear unsteady vorticity field in the cylinder. The present computational results show that unsteady vorticity is generated at the injecting sidewall by an interaction between the injected fluid and the axial pressure gradient arising from a planar acoustic wave field induced by the sidewall injection transients. In the present case, the vorticity is convected away from the wall into the chamber by the spatially distributed unsteady injected flowfield. In previous studies by Zhao et al.[21] and Kirkkopru et al.,[6] where the sidewall injection velocity is spatially uniform and constant, the unsteady vorticity is convected by the simpler steady radial velocity field. For sufficiently short times, a well defined front separates the relatively low vorticity chamber core flow from a region of more intense unsteady vorticity generated initially at the wall. The radial location of the vorticity front varies with axial location because the transient sidewall injection distribution is axially dependent.

Fully resolved, time-dependent results enable one to understand the source and evolution of unsteady vorticity in the system, its ultimate distribution, and the length scales on which it is important. These insights are difficult to extract from the cited previous work because 1) the radial spatial variations in the numerical solutions are not adequately resolved, and 2) the numerical results are frequently presented in time-averaged form, so that the information about the transient evolution of the field variables is lost.

II. Computational Model

The flowfield is described by the cylindrical, axisymmetric, laminar, compressible Navier–Stokes equations, for a perfect gas, written in nondimensional conservative form:

$$\frac{\partial q}{\partial t} + \frac{\partial e}{\partial x} + \frac{\partial f}{\partial r} + \frac{h}{r} = 0 \tag{1}$$

where

$$q = \begin{bmatrix} \rho \\ E_T \\ \rho u \\ \rho v \end{bmatrix} \qquad e = \begin{bmatrix} M\rho u \\ M[E_T + (\gamma - 1)p]u \\ M\rho u^2 + \dfrac{1}{\gamma M} p \\ M\rho uv \end{bmatrix}$$

$$f = \begin{bmatrix} M\rho v \\ M[E_T + (\gamma - 1)p]v - \dfrac{\gamma M\delta^2}{RePr} T_{,r} \\ M\rho uv - \dfrac{M\delta^2}{Re} u_{,r} \\ M\rho v^2 + \dfrac{\delta^2}{\gamma M} p \end{bmatrix} \tag{2}$$

$$h = \begin{bmatrix} M\rho v \\ M[E_T + (\gamma - 1)p]v - \dfrac{\gamma M\delta^2}{RePr} T_{,r} \\ M\rho uv - \dfrac{M\delta^2}{Re} u_{,r} \\ M\rho v^2 \end{bmatrix}$$

$$E_T = \rho C_v T + \gamma(\gamma - 1)M^2 \frac{[u^2 + (v/\delta)^2]}{2} \tag{3}$$

is the total fluid energy.

The equation of state for a perfect gas is

$$p = \rho T \tag{4}$$

Nondimensional variables, defined in terms of dimensional quantities denoted by a prime, are given by

$$\begin{aligned} x &= x'/L' & r &= r'/R' & u &= u'/U'_R \\ v &= v'/V'_R & \rho &= \rho'/\rho'_0 & p &= p'/p'_0 \\ T &= T'/T'_0 & t &= t'/t'_a & C_v &= C'_v/C'_{v0} \end{aligned} \tag{5}$$

Characteristic length scales for the axial and radial directions are chosen to be the length of the tube L' and the radius of the tube R', respectively. The known characteristic sidewall injection speed of the fluid V'_R is related to the characteristic axial speed U'_R through the global mass conservation relationship $U'_R = \delta V'_R$, where $\delta = L'/R'$ is the aspect ratio of the tube. Pressure is nondimensionalized with respect to the static pressure compatible with the injected fluid density and temperature, ρ'_0 and T'_0, respectively. Time is nondimensionalized with respect to the tube axial acoustic time $t'_a = L'/a'_0$, where $a'_0 = (\gamma p'_0/\rho'_0)^{1/2}$ is the characteristic speed of sound. Here, the ratio of specific heats $\gamma = 1.4$ is used in the present computations. The viscosity, specific heats, and conductivity are treated as constants in these calculations, because temperature variations are very small.

The following expressions define the flow Reynolds number, the Prandtl number, and the characteristic axial flow Mach number, respectively:

$$Re = \frac{\rho_0' U_R' L'}{\mu_0'} \qquad Pr = \frac{\mu_0' C_{p0}'}{k_0'} \qquad M = \frac{U_R'}{a_0'} \tag{6}$$

Note that the acoustic Reynolds number $Re_A = Re/M$, and the injection Mach number $M_i = M/\delta$. In a typical solid rocket motor chamber $Re = \mathcal{O}(10^4-10^6)$, $Pr = \mathcal{O}(1)$, $M = \mathcal{O}(10^{-2}-10^{-1})$, and $\delta = \mathcal{O}(10)$.

The Navier–Stokes equations are simplified by ignoring the axial transport terms. Justification for the reduction is based on the asymptotic analysis in Zhao and Kassoy[8] and Zhao et al.[21] valid for $M << 1$, $\delta >> 1$, and $Re >> 1$ provided that the hard blowing condition $\delta^2/Re << 1$ is satisfied. As a result, the computation time is reduced significantly without sacrificing flow physics. Furthermore, the dissipative effects of the remaining transport terms are sufficient to avoid artificial damping terms needed in other similar computations.[15,16,24]

The Navier–Stokes equations are solved by using the two–four explicit, predictor–corrector scheme,[23] which is a fourth-order variant of the fully explicit MacCormack scheme. This method is highly phase-accurate and is therefore very suitable for wave propagation and wave interaction problems. The number of conditions specified on a boundary are equal to the number of characteristics pointing into the computational domain.[7] The remaining numerically required conditions are extrapolated from the computational domain to the boundary.

The size and the number of uniformly spaced grids are chosen to accommodate properly the local variations of flow variables in the axial and radial directions as suggested in the asymptotic analysis by Zhao et al.[21]

A steady-state flow solution is required as an initial condition for the transient flow computation. Boundary conditions include an impermeable head end at $x = 0$ ($u = 0$), an assumed pressure node at the exit plane $x = 1$ ($p = 1$), a specified injection velocity ($v = -1$), temperature ($T = 1$), and a no-slip condition for the axial flow speed ($u = 0$) on the sidewall at $r = 1$ as well as symmetry conditions on the centerline, $r = 0$.

The analytically calculated velocity profiles for incompressible, rotational, inviscid flow in a long, narrow cylindrical tube (Culick[18]) are used as starting profiles for the steady, compressible, viscous flow computations. This approach reduces the computation time required to reach the final converged steady flow configuration relative to doing a complete transient solution by initiating wall injection at $t = 0$. In this calculation the solution converges to a steady state defined by the condition that the total injected mass is equal to the total exiting mass. Then the solution is run for as much as $\mathcal{O}(10)$ additional axial acoustic times to ensure that the steady-state solution is stable. Results given in Fig. 1 show the steady normalized axial, $u_S(x, r)/u_S(x, r = 0)$, and radial velocity $v_S(x, r)$ profiles at different axial locations, $x = 0.025$, 0.5, and 1.0, when $M = 0.06$, $\delta = 20$, and $Re = 10^5$, respectively. In these graphs, Culick[18] incompressible flow profiles that are invariant to axial location are nearly indistinguishable from the computed profiles. Small differences arise from the small but finite axial flow Mach number used in the computation. Low Mach number compressible flow theory implies $\mathcal{O}(M^2)$ differences between the Culick[18] solution for $\delta >> 1$ and the computational result.

A steady-state flow solution for each Mach number and Reynolds number is obtained initially to prevent introducing unwanted noise into the unsteady computations.

Zhao et al.[21] have used formal asymptotic methods to show that the chamber flow is weakly viscous when the condition $Re = \mathcal{O}(\delta^2/M^2)$ is satisfied and when strong injection ($\delta^2/Re << 1$) prevails. The latter condition implies that $V_R' >> U_R'/Re^{1/2}$ (Ref. 22). The asymptotic theory shows that the primary viscous stresses are in the radial direction. Hence, it is useful to ignore the axial transport effects and retain only the radial transport terms in the reduced Navier–Stokes equations. The steady flow solution is obtained faster and, at the same time, the largest important viscous effects in radial direction are responsible for physically meaningful damping, similar to the artificial damping terms that have been introduced in some earlier studies.[15,16,24]

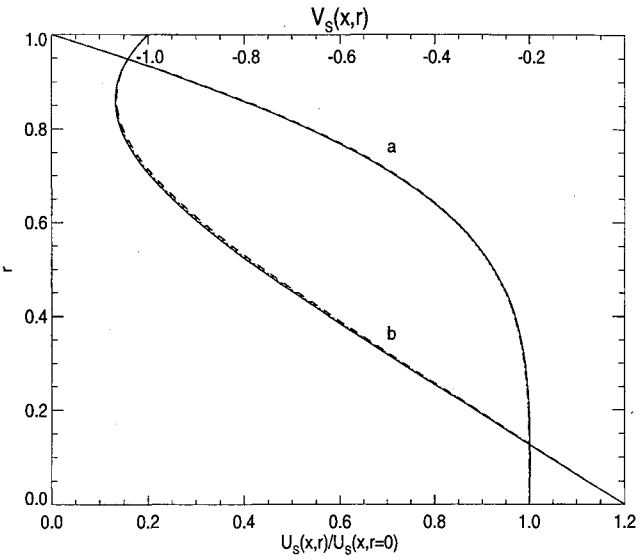

Fig. 1 a) Normalized steady axial velocity and b) steady radial velocity profiles at $x = 0.025$ (solid line), 0.5 (dotted line), and 1 (dashed line) for $M = 0.06$, $Re = 10^5$, and $\delta = 20$.

Once a converged steady flow configuration for specified values of δ, M, and Re is obtained, the flow is disturbed by adding an axially distributed unsteady sidewall injection component to the steady value. The total wall injection velocity is then given by

$$v(x, r = 1, t) = -[1 + A\cos(n\pi x/2)(1 - \cos \omega t)] \tag{7}$$

which can also be written in terms of a positive mean component $1 + A\cos(n\pi x/2)$ and a fluctuating component proportional to $\cos \omega t$. Here ω is the dimensionless angular frequency, $A = \mathcal{O}(1)$ is the amplitude of the unsteady wall injection, and n is the spatial dependence parameter. The total mass flow from the wall is always positive. The other boundary conditions are the same as those for the steady flow computations.

Unsteady computations are carried out for several different axial Mach numbers and spatial dependence parameters. In this study the boundary driving frequency is $\omega = 1$. This is a relatively low frequency in the sense that the period $t = 2\pi$ is larger than the time required for an acoustic wave to do a complete circuit of the chamber, $t = 2$.

III. Results and Discussion

The numerical code has been run approximately 10 cycles after the injection transient is turned on to check if spurious numerical oscillations develop. For example, Fig. 2 shows the time variation of the centerline axial velocity at the midchamber ($x = 0.5$) for flow parameters $M = 0.1$, $\delta = 20$, $Re = 10^5$, $A = 0.4$, $n = 1$, and $\omega = 1$. Note that the value at $t = 0$ corresponds to the steady-state value of the centerline velocity at the midchamber. The solution appears to be quasisteady almost immediately. This solution property can be attributed to the transient pressure field seen in Fig. 3. The result given at $x = 0.5$ shows that pressure solution is almost purely planar (x dependent only). For example, at $x = 0.5$ and $t = 60$ for three radial locations, $r = 0$, 0.5, and 1, $p = 1.1480096$, 1.1479678, and 1.1479073, respectively. The invariance to radial loca-

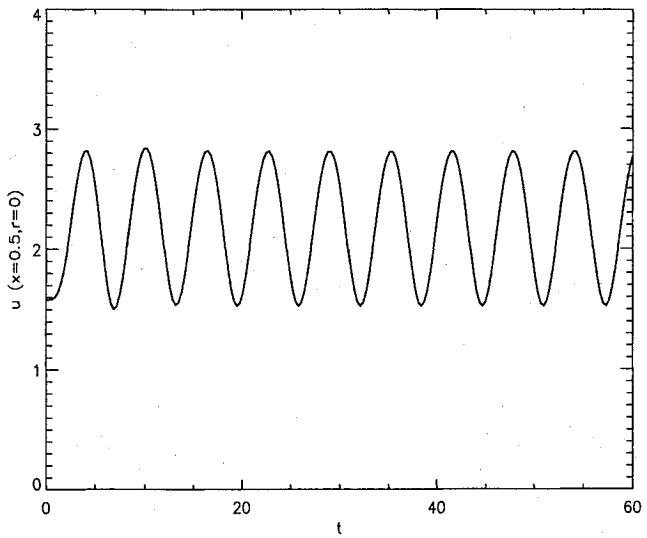

Fig. 2 Time history of the centerline axial velocity at $x = 0.5$ for $M = 0.1$, $\delta = 20$, $Re = 10^5$, $\omega = 1$, $A = 0.4$, and $n = 1$.

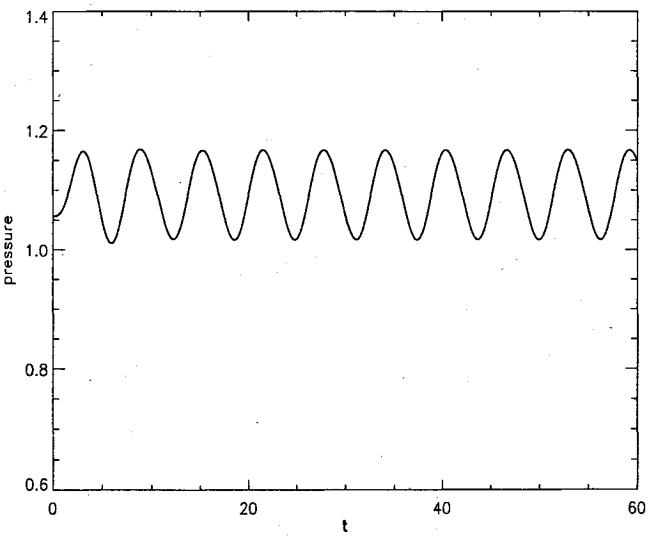

Fig. 3 Time history of pressure at $x = 0.5$ for $M = 0.1$, $\delta = 20$, $Re = 10^5$, $\omega = 1$, $A = 0.4$, and $n = 1$.

tion results from the use of a large aspect ratio $\delta = 20$. Also note that the pressure deviation from the base value, $\mathcal{O}(10^{-1})$, is fully compatible with the asymptotic prediction in Zhao et al.[25]

The purely harmonic behavior in Fig. 3, seen in all similar computational results,[4,7,19] is cause for concern because the analytical analogue to this study[25] shows that a single eigenfunction of substantial amplitude should accompany the forced response. The eigenfunction arises from a solution to a linear, acoustic equation driven by transient effects on the sidewall boundary. In contrast, the numerical solution arises from a slightly viscous, weakly nonlinear mathematical system. It appears that there are at least two possible sources for the difference:

1) The finite difference form of the nonlinear, slightly viscous equations will not produce an eigenvalue-like response.

2) The numerical boundary conditions at the exit plane do not account for wave reflections in an appropriate way.

These issues are the subject of the ongoing studies. Note that acoustic wave planar viscous damping occurs on a time scale $t >> \mathcal{O}(10^2)$ (Ref. 26) for the Reynolds numbers considered here. Hence, on the time scale $t = \mathcal{O}(10^2)$ planar damping cannot annihilate an eigenfunction response.

Following a procedure described by Lagerstrom,[27] and similar to that employed by Flandro and Roach,[15] Zhao and Kassoy,[8] and Zhao et al.,[21] the total unsteady axial flow speed may be divided into three parts

$$u(x, r, t) = u_S(x, r) + u_P(x, t) + u_V(x, r, t) \qquad (8)$$

where u_S denotes the steady flowfield that is known as an initial condition for the unsteady computations. The second term u_P is the weakly viscous, slightly nonlinear analogue to the irrotational planar part of the flowfield found by Zhao et al.[21] and Zhao.[25] It is found from the difference between the unsteady axial speed and the steady axial speed on the centerline of the tube. The remaining term u_V, defined as the rotational (nonplanar) part of the unsteady axial flow speed, is found from Eq. (8) after u_S and u_P are calculated. Once again, it is an analogue to the analytically obtained rotational velocity field described by Zhao et al.[21] and Zhao[25] and is used to describe the generation and evolution of the nonlinear unsteady vorticity field in the cylinder. Following the asymptotic analysis described by Zhao et al.[21] and Zhao[25] one can show that the rotational part of u_V vanishes at the centerline for all times.

Figure 4 shows the radial variation of the instantaneous unsteady axial rotational flow speed u_V at midchamber ($x = 0.5$) for three time values after the injection transient is initiated at the sidewall. The flow parameters are $M = 0.1$, $\delta = 20$, and $Re = 10^5$. The corresponding injection Mach number $M_i = M/\delta = 5 \times 10^{-3}$. The disturbance frequency is $\omega = 1.0$, a nonresonant frequency smaller than the first fundamental frequency of the tube, $\omega_1 = \pi/2$.

One observes a radial velocity gradient (hence vorticity) extending out about 0.35 units from the wall ($r = 1$) at $t = 3.00$ (solid line) and to about 0.65 radial units when $t = 6.00$. At $t = 9.90$ the numerical data themself show that the rotational flowfield has spread throughout the chamber.

The spatial distribution of the rotational part of the unsteady axial flow velocity at each time may be explained in physical terms by considering an interaction between the total unsteady injected flowfield and the axial planar acoustic wave induced and sustained by sidewall injection transients. The motion of a fluid particle injected radially into the tube from the sidewall at a specified axial location is affected by the harmonic variation with time of the local axial planar pressure gradient. For instance, Fig. 5 shows the time variation of the axial pressure

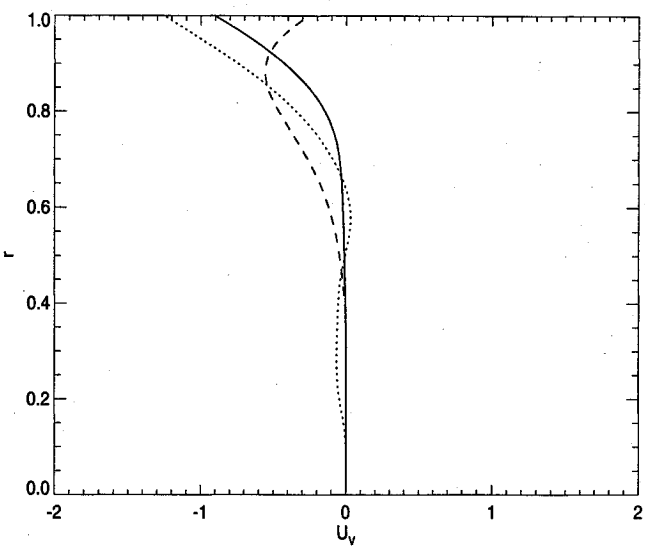

Fig. 4 Radial variation of u_V at $x = 0.5$ when $t = 3$ (solid line), $t = 6$ (dashed line), and $t = 9.9$ (dotted line) for $M = 0.1$, $\delta = 20$, $Re = 10^5$, $\omega = 1$, $A = 0.4$, and $n = 1$.

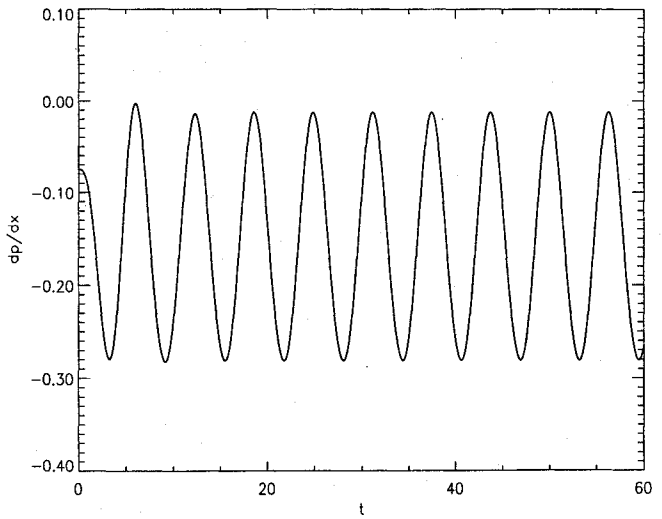

Fig. 5 Time history of axial pressure gradient, $\partial p/\partial x$, at $x = 0.5$, $r = 0.95$ for $M = 0.1$, $\delta = 20$, $Re = 10^5$, $\omega = 1$, $A = 0.4$, and $n = 1$.

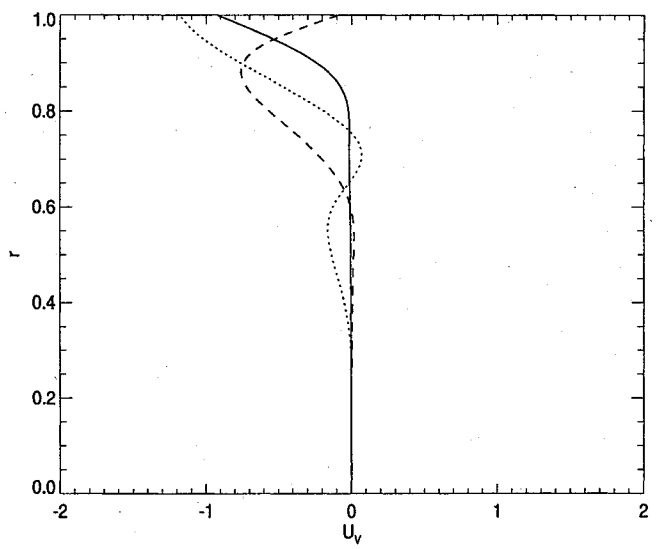

Fig. 6 Radial variation of u_v at $x = 0.5$ when $t = 2.96$ (solid line), $t = 5.92$ (dashed line), and $t = 10.05$ (dotted line) for $M = 0.06$, $\delta = 20$, $Re = 10^5$, $\omega = 1$, $A = 0.4$, and $n = 1$.

gradient, $\partial p/\partial x$, at a point where $x = 0.5$ and $r = 0.95$ for the case being discussed previously. As a result, a given fluid particle emanating from the wall will be accelerated alternately in the positive and negative axial directions as it is convected toward the axis of the cylinder by the unsteady radial flowfield. Part of the fluid particle response is associated with irrotational acoustic effects. The rest is rotational, resulting from vorticity generation at the wall.

Figure 4 shows that by $t = 10$ unsteady vorticity has filled the cylinder. But Fig. 3 shows no change in the r-independent pressure field as vorticity fills the system. It follows that the presence of vorticity does not affect the pressure field, as predicted by Flandro and Roach[15] and in the asymptotic analysis of Zhao et al.[21] and Zhao.[25] This provides an explanation of why traditional acoustic stability theory yields transient pressure estimates that compare well with those found experimentally, although the acoustic velocity field will differ considerably from that observed by Brown et al.[1,2]

Figure 6 shows the instantaneous spatial variation of u_V at $x = 0.5$ with respect to the radius when $t = 2.96$, 5.92, and 10.05 for a smaller axial Mach number $M = 0.06$ (corresponding to the weaker injection, $M_i = 3 \times 10^{-3}$) and for the same $Re = 10^5$. The forcing frequency $\omega = 1.0$ is the same as for the previous case. The amplitude of the nonresonant injection transient disturbance is $A = 0.4$. The sharply defined region of large velocity gradient is seen in Fig. 6 out to about 0.23 units from the wall at $t = 2.96$. One notes that at $t = 5.92$ the wavelength of the spatial oscillation of u_V is smaller than that for the case when $M = 0.1$. This is an expected result because the total unsteady radial velocity field for $M = 0.06$, which transports the fluid particles into the cylinder, is characterized by a relatively lower speed than that for the $M = 0.1$ case. Injected fluid particles are carried a shorter distance away from the sidewall towards the axis in a given time interval, relative to that for the stronger injection speed case, $M = 0.1$. At $t = 10.05$ one notes that spatial oscillations are present about 0.7 radial units from the wall.

Solution resolution requires 41 grid points in the axial direction and 101 grid points in the radial direction in the two cases discussed previously. Figure 6 shows that near the injecting wall one wavelength of the spatial oscillation of u_V is represented by approximately 35–40 radial grid points. In contrast, near the centerline, where the wavelength is smaller, fewer but an adequate number of grid points per wavelength are available to resolve the velocity gradients.

The third case studied is for a smaller characteristic axial flow Mach number $M = 0.02$ ($M_i = 10^{-3}$), $\delta = 20$, slightly larger Reynolds number $Re = 3 \times 10^5$, and the forcing frequency $\omega = 1.0$. The results for the previous cases, $M = 0.1$ and $M = 0.06$, imply that the number of radial grid points should be doubled for this weak injection case. There are 201 equally spaced grid points in the radial direction to represent the spatial variation of u_v accurately. Figure 7 shows the instantaneous variation of u_v with respect to the radius at $x = 0.5$ when $t = 2.99$, 4.93, and 10.00. It can be seen from this figure that axial velocity gradients are larger than those for larger Mach number cases presented previously. This implies that the absolute magnitude of the unsteady vorticity generated at the wall is much larger than that of the higher Mach number flows. This unsteady vorticity field is convected away from the wall towards the center of the chamber by a relatively slower radial velocity component. Therefore, at $t = 10.00$ only about 30% of the chamber is filled with the unsteady vorticity.

Figure 8 shows the instantaneous radial variation of u_V at $x = 0.5$ for larger times, $t = 10.00$, 20.01, 30.02, and 40.02. The computational data can be used to infer that the unsteady vorticity field spreads out toward the axis as time increases, so that eventually the entire cylinder is filled with an intense

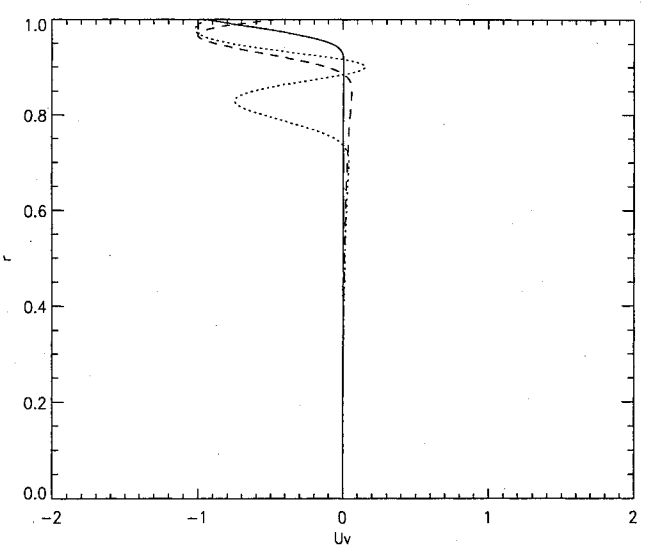

Fig. 7 Radial variation of u_v at $x = 0.5$ when $t = 2.99$ (solid line), $t = 4.93$ (dashed line), and $t = 10.00$ (dotted line) for $M = 0.02$, $\delta = 20$, $Re = 3 \times 10^5$, $\omega = 1$, $A = 0.4$, and $n = 1$.

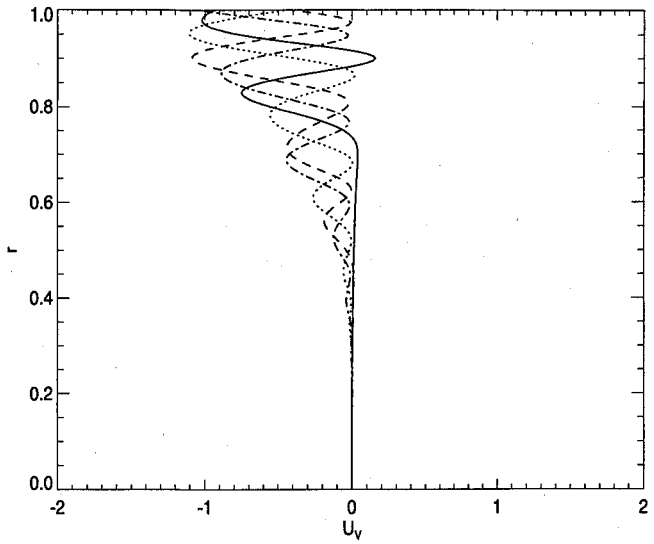

Fig. 8 Same as Fig. 7, but for t = 10.00 (solid line), t = 20.01 (dashed line), t = 30.02 (dotted line), and t = 40.02 (dash–dot line).

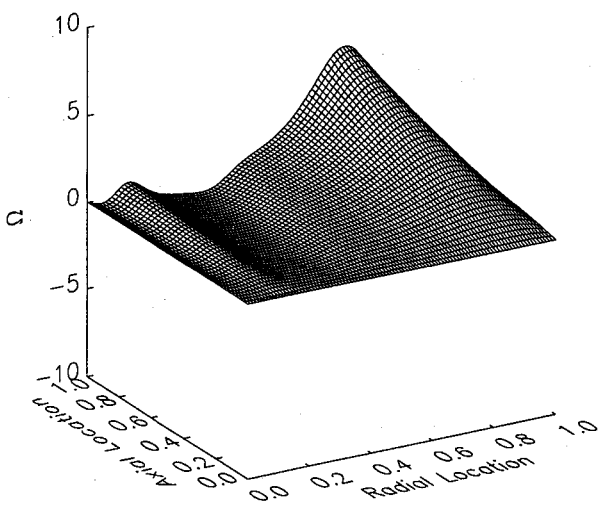

Fig. 9 Spatial variation of the unsteady distribution Ω as a function of axial location and radial location at t = 30 for M = 0.1 and δ = 20.

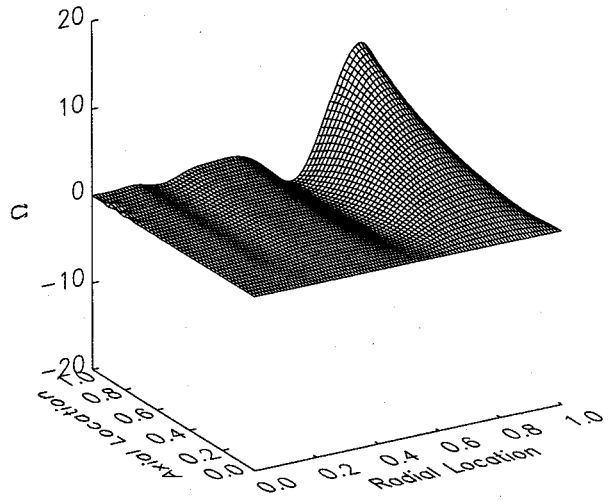

Fig. 10 Same as Fig. 9 but at t = 29.56 and M = 0.06. Note the different scale in Ω.

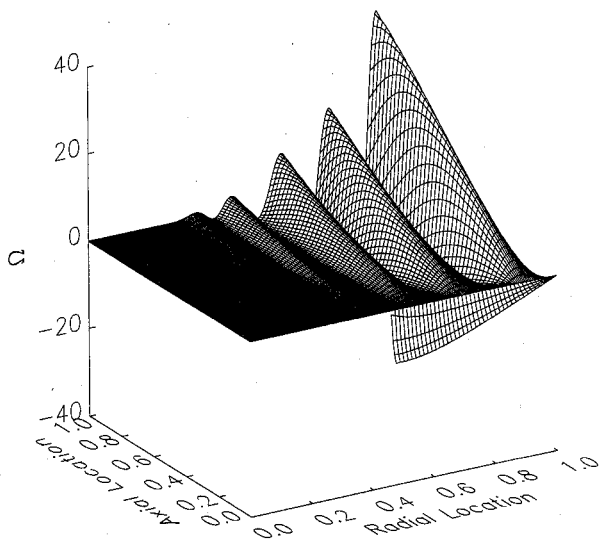

Fig. 11 Same as Fig. 9 but at t = 30.02 and M = 0.02. Note the different scale in Ω.

level of vorticity, approximately $\mathcal{O}(1/M)$ larger than that associated with the u_S velocity field.

Here again, the wavelength of the oscillatory structure decreases as the centerline is approached. This occurs because the rate of radial convection is reduced as the radial velocity component decreases toward zero near the axis of the chamber. The implication for mesh distributions is that there must be adequate spatial resolution throughout the cylinder, not just in an acoustic boundary layer near the injecting surface as used in a variety of earlier computations.[4,7,19] Of course, this necessity arises because the injection velocity is sufficiently large to preclude the existence of a thin localized viscous layer like that considered by Flandro.[5]

Figures 9–11 show the instantaneous unsteady vorticity distribution throughout the chamber for three cases, M = 0.1 (t = 30.00), 0.06 (t = 29.56), and 0.02 (t = 30.02), discussed earlier, where one notes significant variation in the axial direction. The unsteady vorticity is computed from

$$\Omega = -\left[\frac{\partial u_V}{\partial r} - \frac{1}{\delta^2}\frac{\partial (v - v_S)}{\partial x}\right] \tag{9}$$

defined as $\Omega = \Omega'/(U'_R/R')$, where primed quantities are dimensional. The numerical results and the asymptotics of Zhao et al.[21] show that the main contribution to Ω is brought by the first term in Eq. (9). A comparison of Figs. 9–11, with significantly varying vertical scales, shows that the magnitude of Ω increases with decreasing values of M. The distribution of vorticity extends out to axis for the two larger Mach numbers in Figs. 9 and 10. Figure 11 shows a succession of wave-like morphologies extending to about r = 0.3.

Long-time results (t = 52.42) for the M = 0.02 case are given in Figs. 12 and 13 to show that unsteady vorticity eventually fills the entire cylinder, even for a relatively small Mach number. Although the graphical representation of Ω in Fig. 12 appears to imply that there is no vorticity close to the axis, the enlarged scale result in Fig. 13 demonstrates the presence of vorticity waves close to r = 0.

Figure 14 provides the radial variation of the unsteady part of the radial speed, $v - v_S$, at t = 30.02 and x = 0.5 for M = 0.02, δ = 20, $Re = 3 \times 10^5$, n = 1, A = 0.4, and ω = 1. The steady radial velocity v_S, associated with constant wall injection, is shown as curve b in Fig. 1. The result in Fig. 14 corresponds to the axial velocity result in Fig. 8. A study of the numerical data shows that the vorticity front is located about 0.7 radial units from the wall. One may observe considerable spatial variation in the radial speed of the fluid toward the axis when $0.5 \lesssim r \lesssim 1$.

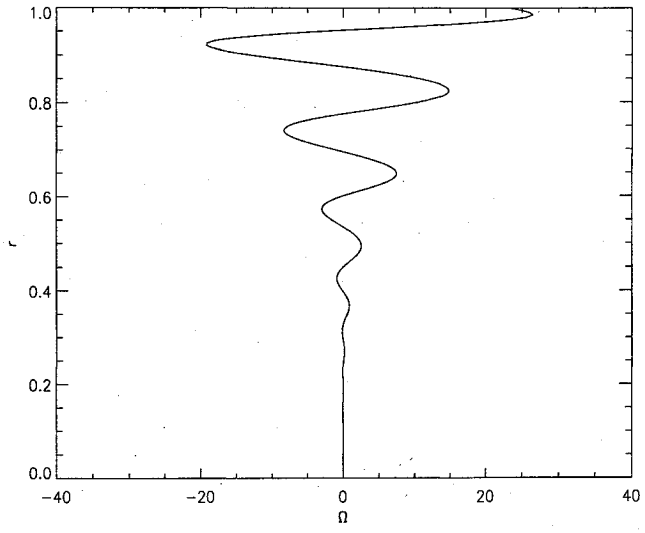

Fig. 12 Radial variation of Ω at $x = 0.5$ when $t = 52.42$ for $M = 0.02$, $Re = 3 \times 10^5$, $\omega = 1$, $A = 0.4$, and $n = 1$.

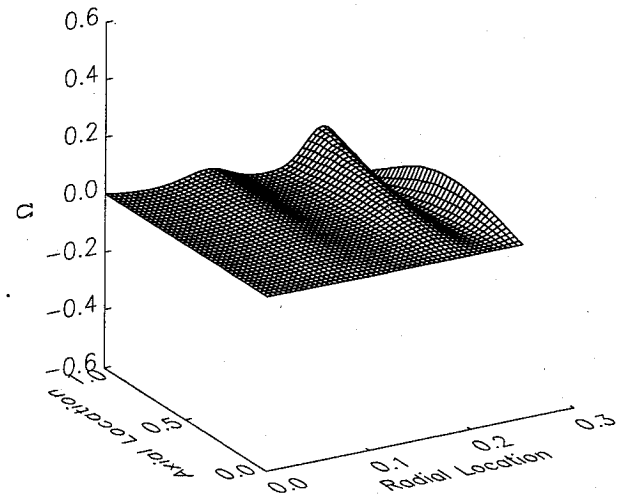

Fig. 13 Unsteady vorticity variation in the region where $0 \leq x \leq 1$, $0 \leq r \leq 0.25$ for the same parameters and time in Fig. 12.

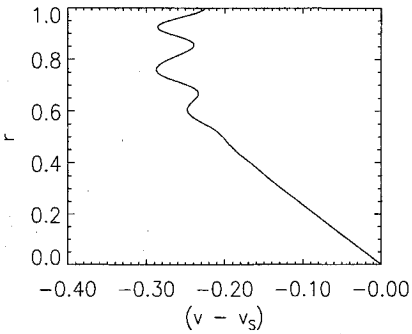

Fig. 14 Instant radial variation of $(v - v_S)$ at $x = 0.5$ when $t = 30.02$ for the same flow parameters as those in Fig. 8.

A more complex wall injection pattern is used to find the results in Figs. 15–18 for the case $n = 3$ in Eq. (7). The vorticity distribution Ω is given for $t = 7.48$, 14.96, 22.44, and 29.92 when $M = 0.02$, $\delta = 20$, $Re = 3 \times 10^5$, $\omega = 1$, and $A = 0.5$. Note that the morphology of the surfaces is considerably more complex than those in Figs. 9–11 and 13 for $n = 1$. These graphs show at a fixed radial location that Ω increases monotonically with axial position when the instantaneous wall injection speed decreases monotonically as x increases [$n = 1$ in Eq. (7)]. The relative increase in the radial gradient of u_V with increasing x can be explained in terms of the vorticity generating interaction between the harmonically varying axial pressure gradient (see Fig. 5) and the fluid injected at a given axial location. In particular, the magnitude of the radial gradient of u_V at the wall depends directly on the radial distance traveled by a fluid particle exiting from the injecting surface during one cycle in $\partial p/\partial x$. Downstream, more slowly moving injected fluid particles will be accelerated and decelerated by the variation in $\partial p/\partial x$ on a shorter radial length scale than those upstream. As a result the radial gradient of u_V is relatively larger at downstream locations.

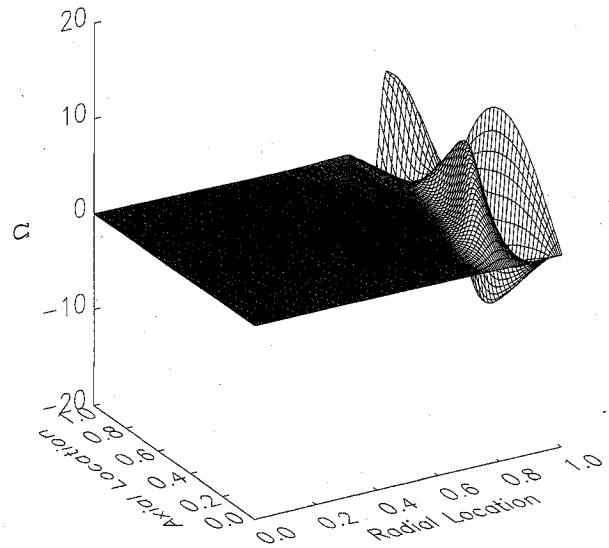

Fig. 15 Instantaneous unsteady vorticity variation throughout the cylindrical chamber at $t = 7.48$ for $M = 0.02$, $\delta = 20$, $Re = 3 \times 10^5$, $\omega = 1$, $A = 0.5$, and $n = 3$. The net mean injection speed in Eq. (7) is always positive.

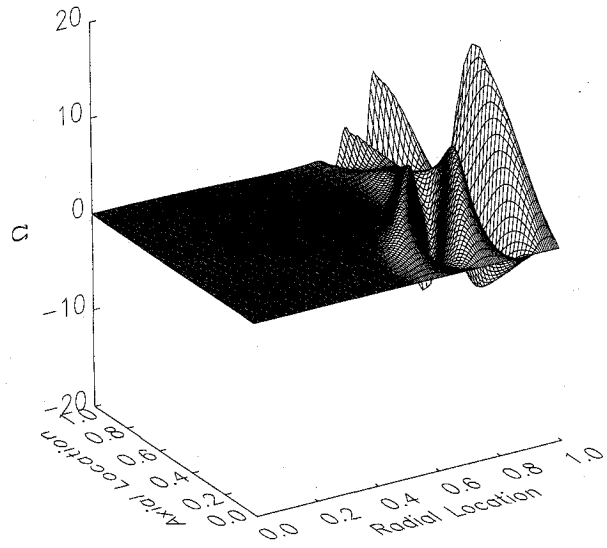

Fig. 16 Same as Fig. 15 but at $t = 14.96$.

In contrast, the corrugated appearance of the surfaces in Figs. 15–18 arises from the variability of the injection speed along the cylinder surface. One may also observe that the radial location of the front is dependent on axial position and reflects the characteristics of the sidewall injection distribution with axial coordinate in x. This implies that the front morphologies can be quite complex if the injection distribution is spatially irregular and complex.

The amplitude of the unsteady vorticity distributions is $\mathcal{O}(M^{-1})$ larger than that of the Culick[18] steady solution, a result

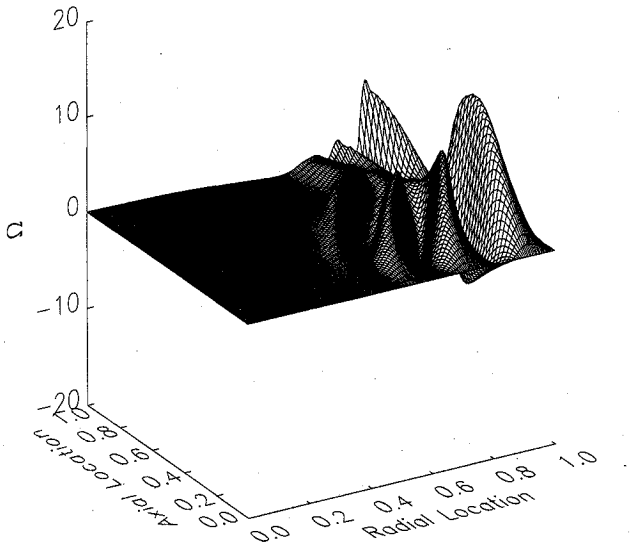

Fig. 17 Same as Fig. 15 but at $t = 22.44$.

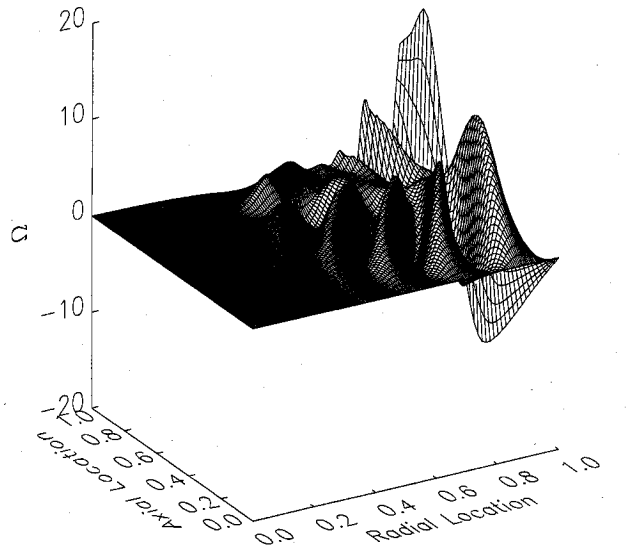

Fig. 18 Same as Fig. 15 but at $t = 29.92$.

predicted by the Zhao et al.[21] and Zhao[25] asymptotic theory. This implies that there will exist a relatively large transient axial shear stress on the sidewall surface, particularly for smaller M values. One can speculate that these large transient shear stresses will impact the burning rate of a solid propellant that is the source of the injected fluid used in the present model. Perhaps there is a direct relationship between the effect of the surface shear stress transients, predicted in the present work, and erosive burning concepts used in the solid rocket engineering literature.[12]

IV. Summary and Conclusions

Unsteady vorticity generation and evolution caused from simulated propellant burning transients in an idealized rocket motor chamber are studied in the context of an initial boundary value problem. An axially distributed, harmonically varying sidewall injection component is superimposed on a similar magnitude steady sidewall injection to simulate spatially variable, time-dependent mass addition from solid propellant burning.

The nearly complete compressible Navier–Stokes equations are solved numerically, using a grid distribution that resolves locally large radial gradients of the axial velocity across the diameter of the cylinder. Instantaneous values of the flow variables are presented to describe the time evolution of unsteady vorticity creation and propagation. This provides an alternative to the studies by Tseng and Yang,[19] Flandro and Roach,[15] Smith et al.,[16] and Tseng et al.,[17] where an acoustic-based time-averaging approach is used to study mean spatial distributions.

The computational analysis shows that axial planar acoustic waves induced and sustained by the sidewall injection transients interact with the sidewall injection induced flow in the chamber to generate unsteady vorticity on the sidewall. This time-dependent vorticity is subsequently convected into the entire chamber by the unsteady radial flowfield. For sufficiently short times, there is a well-defined front that separates the intense transient vorticity generated at the injecting surface from the relatively weak vorticity in the initial steady shear flow.

The instantaneous radial location of the front varies in the axial direction when the wall injection is spatially distributed. In contrast, flows generated by uniform constant sidewall injection, subject to either endwall or exit flow disturbances, have instantaneous front locations that are invariant in the axial direction.[6,8,21]

The maximum amplitude of the intense vorticity, generated at the wall and convected subsequently into the cylinder by the radial component of the flow velocity, scales approximately like $1/M$ (see Figs. 9–11) as predicted by the formal asymptotic analysis in Ref. 25, in the model of Flandro and Roach[15] and Flandro.[17] Near the sidewall, where the rotational part of the axial velocity u_V is relatively small, one finds a large radial gradient as seen in Fig. 8. It is conceivable that these large transient gradients will persist to the surface of a burning solid propellant in a real rocket chamber and the resulting axial shear stresses may affect the characteristics of the combustion process.

The results presented here satisfy the order of magnitude equality $Re = \mathcal{O}(\delta^2/M^2)$ derived by Zhao and Kassoy[8] and Zhao et al.[25] for flows that are weakly, but pervasively viscous. This condition is also satisfied approximately by the parameters used in the computational solutions of Smith et al.[16] and Tseng et al.[7] Note that the equality satisfies the hard-blowing condition of Cole and Aroesty,[22] $Re/\delta^2 >> 1$, so that no thin localized viscous acoustic boundary layer can exist adjacent to the injecting surface. Rather, in this case of a confined geometry the viscous effect is present at a relatively low level across the entire cylinder on the $\mathcal{O}(M)$ length scale of the axial velocity radial gradient.

There is now a considerable body of evidence [1,2,4,6,17,19–21,25] in support of the presence of an intense unsteady vorticity distribution within a physically reasonable model of a solid rocket motor chamber. In principle, the basic rotationality of the flowfield should impact traditional irrotational acoustic stability theories. The latter appear to predict acoustic pressure fields seen in solid rocket engines, but are unlikely to give accurate descriptions of axial and radial velocity fields that possess significant rotationality as seen in the work by Brown et al.[1,2]

Acknowledgment

This work is supported by the U.S. Air Force Office of Scientific Research through Grant AFOSR 89-0023.

References

[1]Brown, R. S., Blackner, A. M., Willoughby, P. G., and Dunlap, R., "Coupling Between Acoustic Velocity Oscillations and Solid Propellant Combustion," *Journal of Propulsion and Power*, Vol. 2, No. 5, 1986, pp. 428–437.

[2]Brown, R. S., Blackner, A. M., Willoughby, P. G., and Dunlap, R., "Coupling Between Velocity Oscillations and Solid Propellant Combustion," AIAA Paper 86-0531, Jan. 1986.

[3]Brown, R. S., and Shaeffer, C. W., "Oscillatory Internal Flow Field Studies," U.S. Air Force Office of Scientific Research Contractors Meeting in Propulsion, La Jolla, CA, June 1992.

[4]Vuillot, F., and Avalon, G., "Acoustic Boundary Layers in Solid Propellant Rocket Motors Using Navier-Stokes Equations," *Journal of Propulsion and Power*, Vol. 7, No. 2, 1991, pp. 231–239.
[5]Flandro, G. A., "Solid Propellant Admittance Correction," *Journal of Sound and Vibration*, Vol. 36, No. 3, 1974, pp. 297–312.
[6]Kirkkopru, K., Kassoy, D. R., and Zhao, Q., "Unsteady Vorticity Generation and Evolution in a Long Narrow Cylinder with Sidewall Injection," *Physics of Fluids* (submitted for publication).
[7]Tseng, C., Tseng, I. S., Chu, W., and Yang, V., "Interactions Between Acoustic Waves and Premixed Flames in Porous Chambers," AIAA Paper 94-3328, June 1994.
[8]Zhao, Q., and Kassoy, D. R., "The Generation and Evolution of Unsteady Vorticity in a Solid Rocket Engine Chamber," AIAA Paper 94-0779, Jan. 1994.
[9]Grad, H., "Resonance Burning in Rocket Motors," *Communications on Pure and Applied Mathematics Composites*, Vol. 2, No. 3, 1949, pp. 79–102.
[10]Culick, F. E. C., "Some Recent Results for Nonlinear Acoustics in Combustion Chambers," AIAA Paper 90-3927, Oct. 1990.
[11]Hart, R. W., and McClure, F. T., "Theory of Acoustic Instability in Solid Propellant Rocket Combustion," *10th International Symposium on Combustion*, The Combustion Inst., Pittsburgh, PA, 1965, pp. 1047–1065.
[12]Williams, F. A., *Combustion Theory*, Benjamin/Cummings, Menlo Park, CA, 1985.
[13]Baum, J. D., and Levine, J. N., "Numerical Investigation of Acoustic Refraction," *AIAA Journal*, Vol. 25, No. 12, 1987, pp. 1577–1586.
[14]Baum, J. D., "Energy Exchange Mechanisms Between the Mean and Acoustic Fields in a Simulated Rocket Combustor," U.S. Air Force Office of Scientific Research Contractors Meeting, Atlanta, GA, June 1990.
[15]Flandro, G. A., and Roach, R. L., "Effects of Vorticity Production on Acoustic Waves in a Combustion Chamber," Final Tech. Rept., U.S. Air Force Office of Scientific Research 90-0159, 1992.
[16]Smith, T. M., Roach, R. L., and Flandro, G. A., "Numerical Study of the Unsteady Flow in a Simulated Solid Rocket Motor," AIAA Paper 93-0112, Jan. 1993.
[17]Flandro, G. A., "Effects of Vorticity on Rocket Combustion Stability," *Journal of Propulsion and Power*, Vol. 11, No. 4, 1995, pp. 607–625.
[18]Culick, F. E. C., "Rotational Axisymmetric Mean Flow and Damping of Acoustic Waves in a Solid Propellant Rocket," *AIAA Journal*, Vol. 4, No. 8, 1966, pp. 1462–1464.
[19]Tseng, I. S., and Yang, V., "Interactions of Homogeneous Propellant Combustion and Acoustic Waves in a Solid Rocket Motor," AIAA Paper 92-0101, Jan. 1992.
[20]Roh, T. S., and Yang, V., "Transient Combustion Responses of Solid Propellants to Acoustic Disturbances in Rocket Motors," AIAA Paper 95-0602, Jan. 1995.
[21]Zhao, Q., Kassoy, D. R., and Kirkkopru, K., "Nonlinear Unsteady Vorticity Generation in a Model of a Solid Rocket Engine Chamber," *Journal of Fluid Mechanics* (to be published).
[22]Cole, J. D., and Aroesty, J., "The Blowhard Problem-Inviscid Flows with Surface Injection," *International Journal of Heat and Mass Transfer*, Vol. 11, No. 7, 1968, pp. 1167–1183.
[23]Gottlieb, D., and Turkel, E., "Dissipative Two-Four Methods for Time-Dependent Problems," *Journal of Mathematics of Computation*, Vol. 30, No. 136, 1976, pp. 703–723.
[24]Lupaglazoff, N., and Vuillot, F., "Two-Dimensional Numerical Simulation of the Stability of a Solid Propellant Rocket Motor," AIAA Paper 91-0205, Jan. 1991.
[25]Zhao, Q., "Nonlinear Acoustic Processes in Solid Rocket Engines," Ph.D. Dissertation, Univ. of Colorado, Boulder, CO, 1994.
[26]Landau, L. D., and Lifshitz, E. M., *Fluid Mechanics*, Pergamon, New York, 1959.
[27]Lagerstrom, P. A., *Theory of Laminar Flows*, edited by F. K. Moore, Sec. B, Princeton Univ. Press, Princeton, NJ, 1964.